Statistics of curvature in the submesoscale surface ocean

--Manuscript Draft—

Full Title:	Statistics of curvature in the submesoscale surface ocean
Article Type:	Article
Corresponding Author:	Leo Middleton University of Gothenburg, Sweden
Order of Authors:	Leo Middleton
	Andrey Shcherbina
	J.T. Farrar
Abstract:	Ocean submesoscale (1—10 km) variability is hypothesised to contribute substantially to upper-ocean vertical exchange and heat fluxes, but the three-dimensional turbulent nature of the variability makes it difficult to interpret submesoscale variability dynamically. Statistics of velocity gradients are often analyzed to characterize the nature of submesoscale dynamics. Previous analyses show that intense convergence is concentrated in strain-dominated regions and have commonly associated these regions with fronts; however, straining can have many different forms, so strain dominance is not uniquely diagnostic of frontogenesis. Here, we introduce a flow-following (natural-coordinate) decomposition of the horizontal velocity gradients that separates vorticity and divergence into four components: shearing, curving, extension, and confluence/diffluence. We apply this decomposition to airborne Doppler scatterometer surface velocities, surface drifter trajectories, and a data-assimilating Navy Coastal Ocean Model simulation from the Submesoscale Ocean Dynamics Experiment (S-MODE). Across these datasets we find a pronounced cyclonic asymmetry not only in vorticity but also in its shearing and curving, implying that submesoscale strain asymmetry reflects both shear-dominant and curvature-dominant kinematics. Using idealised representations of surface quasi-geostrophic dynamics, Garrett--Munk internal waves, and wind-driven inertial oscillations, we show that these processes occupy distinct regions of the joint distributions, providing a conceptual dynamical basis for interpreting observed velocity-gradient statistics.

Statistics of curvature in the submesoscale surface ocean

Leo Middleton,[a,c] , Andrey Shcherbina,[b] J. Thomas Farrar,[c]

[a] *University of Gothenburg, Göteborg, Sweden*
[b] *Applied Physics Laboratory, University of Washington, Seattle, WA, USA*
[c] *Woods Hole Oceanographic Institute, Woods Hole, MA, USA*

ABSTRACT: Ocean submesoscale (1–10 km) variability is hypothesised to contribute substantially to upper-ocean vertical exchange and heat fluxes, but the three-dimensional turbulent nature of the variability makes it difficult to interpret submesoscale variability dynamically. Statistics of velocity gradients are often analyzed to characterize the nature of submesoscale dynamics. Previous analyses show that intense convergence is concentrated in strain-dominated regions and have commonly associated these regions with fronts; however, straining can have many different forms, so strain dominance is not uniquely diagnostic of frontogenesis. Here, we introduce a flow-following (natural-coordinate) decomposition of the horizontal velocity gradients that separates vorticity and divergence into four components: shearing, curving, extension, and confluence/diffluence. We apply this decomposition to airborne Doppler scatterometer surface velocities, surface drifter trajectories, and a data-assimilating Navy Coastal Ocean Model simulation from the Submesoscale Ocean Dynamics Experiment (S-MODE). Across these datasets we find a pronounced cyclonic asymmetry not only in vorticity but also in its shearing and curving, implying that submesoscale strain asymmetry reflects both shear-dominant and curvature-dominant kinematics. Using idealised representations of surface quasi-geostrophic dynamics, Garrett–Munk internal waves, and wind-driven inertial oscillations, we show that these processes occupy distinct regions of the joint distributions, providing a conceptual dynamical basis for interpreting observed velocity-gradient statistics.

SIGNIFICANCE STATEMENT: Ocean circulation features between 1 - 10 km in horizontal extent are thought to play a major role in the vertical exchange of ocean tracers. These circulation features have complex topology of jets, eddies, meanders, and spirals – all linked to the underlying dynamics. Here, we explore new methods of statistical characterization of the velocity field features and link it to the dynamics. Unlike the traditional approach that operates in a cartesian frame of reference, we adopt a flow-following reference frame, which decomposes the ocean velocity into flow speed and flow direction. We analyse observational data from the Submesoscale Ocean Dynamics Experiment (S-MODE), a field campaign off the coast of California. Large straight fronts are implicated as the primary regions of intense convergence, but there is also a zoo of curved fronts and eddy structures that play an important role in structuring convergence at small scales.

1. Introduction

Developments in observing and modeling technology have allowed the quantification of submesoscale (1-10 km) ocean dynamics in recent years (e.g. Archer et al. 2025; Middleton et al. 2025; Srinivasan et al. 2023). High-resolution numerical studies have suggested that the global submesoscale contribution to vertical heat fluxes in the upper ocean may be five times as large as the mesoscale contribution (Su et al. 2018). Beyond heat fluxes, submesoscales also shape the structure of ocean ecosystems, forming the patchiness of biogeochemical observations (Mahadevan 2016; Lévy et al. 2018). Grasping the impacts and feedbacks of climate change on ecosystems will require a firm understanding of submesoscale dynamics and how it shapes tracers at these scales.

One reason that vertical fluxes are so enhanced at the submesoscale is the frequent occurrence of intense density fronts (Whalen and Drushka 2025). Fronts are an emergent feature of rotating stratified flows which are particularly intensified at small scales, when Rossby numbers $Ro = U/fL$ become $O(1)$ (Thomas et al. 2008). Fronts sustain ageostrophic secondary circulations that can enhance vertical fluxes of tracers through the water column, in addition to providing an isopycnal connection between the upper ocean and the ocean surface, on which along-isopycnal stirring can force vertical exchange. Fronts can also become unstable to baroclinic instability, giving rise to mixed-layer eddies which can stir tracers laterally and facilitate further vertical fluxes (Spall 1995).

Submesoscale flow fields are turbulent and complex, and so do not necessarily fit into a simple classification of coherent structures like frontal jets and eddies. Because these processes are inherently tied to strong velocity gradients, diagnostics based on velocity-gradient statistics have become a primary tool for identifying submesoscale dynamics in observations and models. Traditionally, the horizontal velocity-gradient tensor is summarized using a small set of coordinate-free quantities, including relative vorticity ζ, horizontal divergence δ, and strain σ. At submesoscales, these quantities become relatively large, often reaching and exceeding the Coriolis parameter i.e.

Corresponding author: Leo Middleton, leo.middleton@gu.se

$O(\zeta/f) \sim 1$ and $O(\delta/f) \sim 1$ for $\zeta = \partial_x v - \partial_y u$ the vertical component of relative vorticity and $\delta = \partial_x u + \partial_y v$ the horizontal divergence, which illustrates their large Rossby number, and potential for ageostrophic dynamics.

Starting with Shcherbina et al. (2013), considering the joint probability density function (PDF) of the velocity gradients, and conditionally averaging various quantities based on these distributions (Balwada et al. 2022) has allowed quantitative statements about chaotic flow fields. Shcherbina et al. (2013) showed that there is a strong asymmetry between cyclonic and anti-cyclonic vorticity at submesoscales, where intense cyclonic vorticity $\zeta > f$ is much more common than anti-cyclonic vorticity $\zeta < -f$. Large cyclonic vorticity is concentrated in regions where the strain magnitude $\sigma = \sqrt{(\partial_x v + \partial_y u)^2 + (\partial_x u - \partial_y v)^2}$ is equal to the vorticity ($\zeta = \sigma$). The regions of strong strain and vorticity were associated with shearing frontal systems. Balwada et al. (2022) showed that regions in which strain dominates over vorticity are responsible for most of the surface convergence $\delta < 0$, and subsequent tracer fluxes. In both these manuscripts, strain dominance was interpreted as evidence of frontal dynamics. However, straining flows can take many forms, which we will demonstrate in section 2b, so there is not a one-to-one relationship between straining and frontogenesis. As a result, existing strain-based statistics cannot uniquely distinguish frontal dynamics from other submesoscale processes.

There is also an asymmetry in divergence observed at submesoscales. Averaged over a sufficiently large area, the vertical volume flux is negligible, so the averaged divergence is near-zero. However, at submesoscales the divergence can become large, and submesoscale-resolving models show more intense, localized convergent regions ($\delta < 0$), balanced by larger scale, weakly divergent regions ($\delta > 0$). For this reason, there has been a search for regions of 'subduction', where surface mixed layer water gets subducted within intensely convergent regions. In addition to subduction of surface water at fronts, a variety of authors have implicated regions with high flow curvature as potential hotspots for subduction (Bower and Rossby 1989; MacKinnon et al. 2021; Pallàs-Sanz et al. 2010; Buckingham et al. 2021; Middleton et al. 2025; Wu et al. 2025). These observations raise the possibility that geometrical features other than straight fronts–particularly strongly curved flows–may play a systematic role in organizing submesoscale convergence.

Flow 'curvature' here refers to the curvature of streamlines or trajectories of the velocity field, defined formally in section 2a. In cylindrical coordinates, or in a flow-following frame, the streamline curvature appears as an advection term normal to the flow direction, adding a centripetal acceleration that either counters or aids the Coriolis force (Shakespeare 2016). More heavily curved regions have a different set of possible force balances that alter the dynamics of instabilities (Buckingham et al. 2021), eddies and frontogenesis (Wu et al. 2025) or subduction (Middleton et al. 2025; MacKinnon et al. 2021). We will investigate the hypothesis that highly curved regions are associated with significant convergence and divergence using the flow-following frame.

To distinguish between frontal dynamics and other strain-producing processes, it is useful to revisit how velocity gradients enter classical theories of frontogenesis. A useful way to define frontogenesis is as a simultaneous increase in both the horizontal buoyancy and velocity gradients (McWilliams 2021). This encompasses the 'classical' models of frontogenesis proposed by Hoskins (1982), where a strain field applied to a horizontal buoyancy gradient with some vertical structure leads to an ageostrophic frontogenetic feedback. This feedback, left undisturbed by along-front instabilities or the effects of turbulence, creates a finite-time singularity (Barkan et al. 2019), so various studies have attempted to answer the question of what the limiting factor on frontogenesis is within the real ocean (Sullivan and McWilliams 2018).

In this manuscript, we add another tool to the statistical analysis of submesoscale flows: decomposing velocity gradients into their curving, shearing, extension and confluent components using a flow-following reference frame (also known as 'natural coordinates'), which separates velocity gradients according to their geometry relative to the flow, as has been done profitably within the atmospheric literature (Bell and Keyser 1993; Viúdez and Haney 1997; Holton and Hakim 2012). We use data from the Submesoscale Ocean Dynamics Experiment (S-MODE): a multi-institution, NASA funded project to comprehensively measure submesoscale dynamics (Farrar et al. 2025). This experiment involved three field campaigns in the California Current region, including in-situ autonomous vehicles, ship-based sampling and airborne observations. The benefit of using this dataset to analyze velocity gradients is that there are multiple consistent and collocated measurements of velocity gradients, both surface and sub-surface. To extend our analysis beyond the observations, we will also use the data-assimilating Navy Coastal Ocean Model (NCOM, D'Addezio and Jacobs 2022), for the region.

We will first introduce the theoretical framework in section 2, i.e. the flow-following reference frame, and its application to submesoscale dynamics. We then go on to introduce a selection of data sources from across the S-MODE campaign (DopplerScatt, NCOM and ocean drifters) in section 3. In section 4 we then present joint PDFs of velocity gradients in a flow-following reference frame, intercompared across our data sources, to create a comprehensive view of curvature statistics and their dynamical interpretation. We go on to discuss the statistics of velocity gradients in a variety of idealised models in section 5 (surface quasi-geostrophy, Garrett-Munk internal gravity waves and wind-driven flow), to help interpret the general results of our statistical analysis. Finally, we

discuss the utility of curvature-based decompositions, and potential routes forward for idealized modeling and observational targeting.

2. Theory

a. Flow-following frame

To account for realistic flow fields with varying curvature, we will use a flow-following reference frame. This formalism is also known as 'natural coordinates', however for arbitrary flows, the velocity field does not necessarily define a true 'coordinate system'. We follow the arguments of Viúdez and Haney (1997), who argue that authors should be explicit when using directional derivatives to make it clear that the formalism is of a 'frame' rather than a coordinate system[1].

The flow-following frame leaves the vertical coordinate as a cartesian coordinate, but replaces the horizontal Cartesian derivatives ∂_x and ∂_y with the directional derivatives

$$\nabla_s \equiv \frac{\boldsymbol{u}_h}{|\boldsymbol{u}_h|} \cdot \nabla_h = \hat{\boldsymbol{s}} \cdot \nabla_h, \tag{1}$$

$$\nabla_n \equiv \left(\boldsymbol{k} \times \frac{\boldsymbol{u}_h}{|\boldsymbol{u}_h|} \right) \cdot \nabla_h = \hat{\boldsymbol{n}} \cdot \nabla_h, \tag{2}$$

in the reference frame defined by the unit vectors $(\hat{\boldsymbol{s}}, \hat{\boldsymbol{n}}, \hat{\boldsymbol{k}})$, where $\hat{\boldsymbol{s}}$ denotes the along-flow direction, $\hat{\boldsymbol{n}}$ denotes the across-flow direction and $\hat{\boldsymbol{k}}$ is the vertical direction, as shown in Figure 1. Note we have avoided using the notation ∂_s and ∂_n as in Bell and Keyser (1993), to avoid implying that $(\hat{\boldsymbol{s}}, \hat{\boldsymbol{n}}, \hat{\boldsymbol{k}})$ define a coordinate system. The horizontal part of the velocity field can then be written $\boldsymbol{u}_h = V\hat{\boldsymbol{s}}$, where we write the speed $V = \sqrt{u^2 + v^2}$ and $\hat{\boldsymbol{s}}$ can be fully described by the scalar angle field α.

The angle field α denotes the angle that the horizontal velocity vector makes with due east i.e. the 'x-axis' (in radians). However, we only ever use derivatives of α, which can be written as

$$\nabla_s \alpha \equiv \hat{\boldsymbol{k}} \cdot \nabla_h \times \hat{\boldsymbol{s}}, \tag{3}$$

$$\nabla_n \alpha \equiv \nabla_h \cdot \hat{\boldsymbol{s}}, \tag{4}$$

In Appendix A, we have given the Cartesian expressions for these derivatives, useful for computation. Starting with the rotating Euler equations, i.e. the frictionless horizontal momentum equations, we can re-express them in the $\hat{\boldsymbol{s}}$ and $\hat{\boldsymbol{n}}$ directions (Bell and Keyser 1993). Including the incompressibility condition, we get

$$\frac{\partial V}{\partial t} + V\nabla_s V + w\frac{\partial V}{\partial z} = -\nabla_s p, \tag{5}$$

$$V\left(\frac{\partial \alpha}{\partial t} + V\nabla_s \alpha + w\frac{\partial \alpha}{\partial z} \right) + fV = -\nabla_n p, \tag{6}$$

$$\frac{\partial w}{\partial t} + V\nabla_s w + w\frac{\partial w}{\partial z} = -\frac{\partial p}{\partial z}, \tag{7}$$

$$\nabla_s V + V\nabla_n \alpha + \frac{\partial w}{\partial z} = 0, \tag{8}$$

where p is the normalized pressure. The first equation describing the momentum balance in the $\hat{\boldsymbol{s}}$-direction determines the flow speed, and the second equation, in the $\hat{\boldsymbol{n}}$-direction determines the flow direction. The equation for w is not impacted by our re-expression in a flow-following frame. Turbulent viscosity terms are easily incorporated into this frame, but we make no use of them in this manuscript.

The Coriolis force only affects the evolution of the flow direction, acting perpendicular to the flow. The radius of curvature of *streamlines* is then expressed exactly as

$$R_s = 1/\nabla_s \alpha, \tag{9}$$

and the radius of curvature of *trajectories* is

$$R_t = V \left/ \frac{D\alpha}{Dt} \right. . \tag{10}$$

Note that both these radii can be computed directly from the Cartesian spatial and temporal velocity gradients (see Appendix A). These definitions give rise to the 'cyclogeostrophic balance' form of Eq. 6,

$$\frac{V^2}{R} + fV = -\frac{\partial p}{\partial r}, \tag{11}$$

by neglecting the vertical velocity, (and assuming the flow-following frame can be treated as a coordinate system, turning the RHS into a partial derivative). When cyclogeostrophic balance is used, the force balance in the $\hat{s}$-direction is explicitly ignored.

The flow direction field α is characterized by both the curvature of streamlines $\kappa_s = 1/R_s = \nabla_s \alpha$ and the variability of α across streamlines $\nabla_n \alpha$. In this manuscript we will use the term curvature only for the curvature of streamlines. The flow speed field V can also be understood as the square root of horizontal kinetic energy $E_k = \frac{1}{2}\boldsymbol{u}_h \cdot \boldsymbol{u}_h = \frac{1}{2}V^2$, so to describe the horizontal flow we need both the distribution of kinetic energy, and information on the flow geometry, contained in the angle field α.

[1] In a coordinate system, one can define partial derivatives e.g. ∂/∂_n and ∂/∂_s that commute, however in general $\nabla_s \nabla_n \neq \nabla_n \nabla_s$ for directional derivatives.

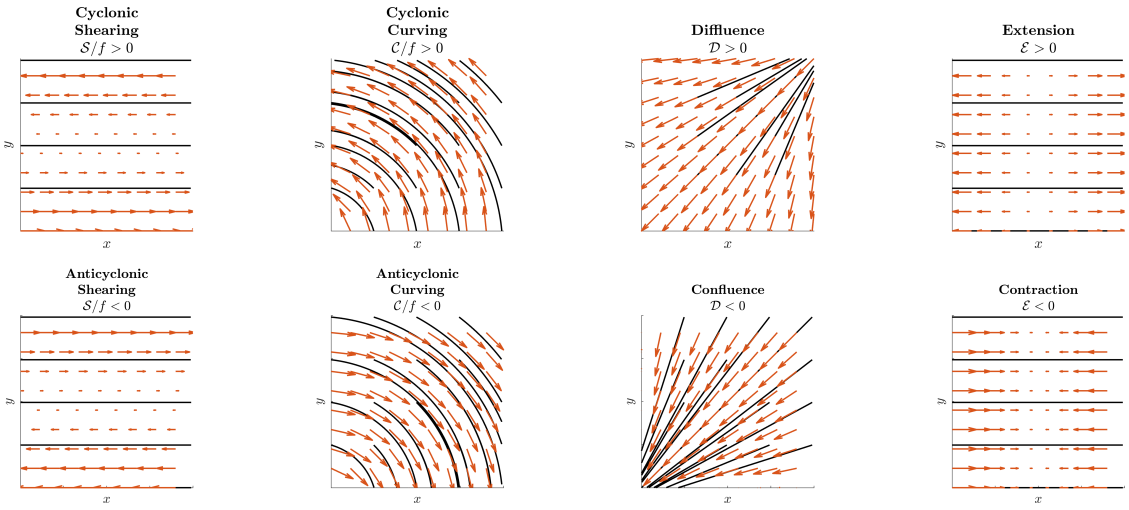

FIG. 1. Example flow fields for the four velocity gradient components in a flow-following frame, presented with both possible signs. Shearing and Curving can be cyclonic or antcyclonic, so are presented normalized by the Coriolis parameter f (i.e. the flow direction will reverse in the Southern hemisphere).

b. *Velocity gradient decomposition*

To understand the effects of curvature on velocity gradients, we can look at the decomposition of vorticity and divergence in terms of direction derivatives (easily verified using the Cartesian expressions in Appendix A)

$$\zeta = -\nabla_n V + V\nabla_s \alpha, \tag{12}$$
$$\delta = \nabla_s V + V\nabla_n \alpha. \tag{13}$$

There are four derivatives in this reference frame, to mirror the terms $\partial_x u, \partial_y u, \partial_x v, \partial_y v$ in Cartesian coordinates. Individually they represent

$$\mathfrak{s} = -\nabla_n V \quad (\text{'shearing'}) \tag{14}$$
$$\mathfrak{c} = V\nabla_s \alpha \quad (\text{'curving'}) \tag{15}$$
$$\mathfrak{e} = \nabla_s V \quad (\text{'extension'/'contraction'}) \tag{16}$$
$$\mathfrak{d} = V\nabla_n \alpha \quad (\text{'diffluence'/'confluence'}) \tag{17}$$

We have defined the sign of these quantities to coincide with those of vorticity, i.e. $\mathfrak{s} > 0$ denotes cyclonic shearing ($\mathfrak{s} < 0$ anticyclonic shearing) and $\mathfrak{c} > 0$ denotes cyclonic curving ($\mathfrak{c} < 0$ anticyclonic curving). Likewise, $\mathfrak{e} > 0$ denotes extension ($\mathfrak{e} < 0$ contraction) and $\mathfrak{d} > 0$ denotes diffluence ($\mathfrak{d} < 0$ confluence), to coincide with the definition of divergence δ. We have illustrated idealized versions of these flows in Figure 1. These components then give a natural decomposition of our strain field into two components that we call the rotational strain and the dilational strain respectively,

$$\sigma_\zeta = \nabla_n V + V\nabla_s \alpha = \mathfrak{c} - \mathfrak{s}, \tag{18}$$
$$\sigma_\delta = -\nabla_s V + V\nabla_n \alpha = \mathfrak{d} - \mathfrak{e}. \tag{19}$$

A classic hyperbolic strain field requires a mixture of σ_ζ and σ_δ, so we have illustrated the relative roles of each component on a hyperbolic strain field in Figure 2. These two strain components have the property that their total magnitude is the same as the total strain $\sigma = \sqrt{\sigma_\zeta^2 + \sigma_\delta^2}$, but represent more meaningful quantities than the Cartesian strain components: 'normal strain' $\sigma_n = \partial_x v + \partial_y u$ and 'shear strain' $\sigma_s = \partial_x u - \partial_y v$, which are simply projections of the strain on two different axes unrelated to the flow geometry. On the other hand, while σ_ζ and σ_δ are also projections, the axes of those are tied to the flow.

Expressing the strain in the flow-following frame helps us intuitively understand straining. Usually strain is imagined as a hyperbolic flow field, but using individual strain components, as visualised in Figure 2, we can create 'eddy-like' flows, that have no vorticity, but do have rotational strain with large $V\nabla_s \alpha$, as long as the shearing exactly compensates the curving. Likewise we can create flows with significant confluence $V\nabla_n \alpha$, but no convergence, if the extension $\nabla_s V$ exactly compensates the confluence, giving a non-zero dilational strain. Strain can be cyclonic or anticyclonic, depending on the sign of the rotational strain, and diffluent or confluent depending on the sign of the dilational strain. We have included budgets for the two strain components in Appendix A.

c. *Fronts*

The dominant dynamics of ocean fronts can be described by simplified idealized models. The most common version of such a model is described by Hoskins (1982) and then refined by Barkan et al. (2019). In this frontal model, the initial system is set up in a quasi-2D state, where all the

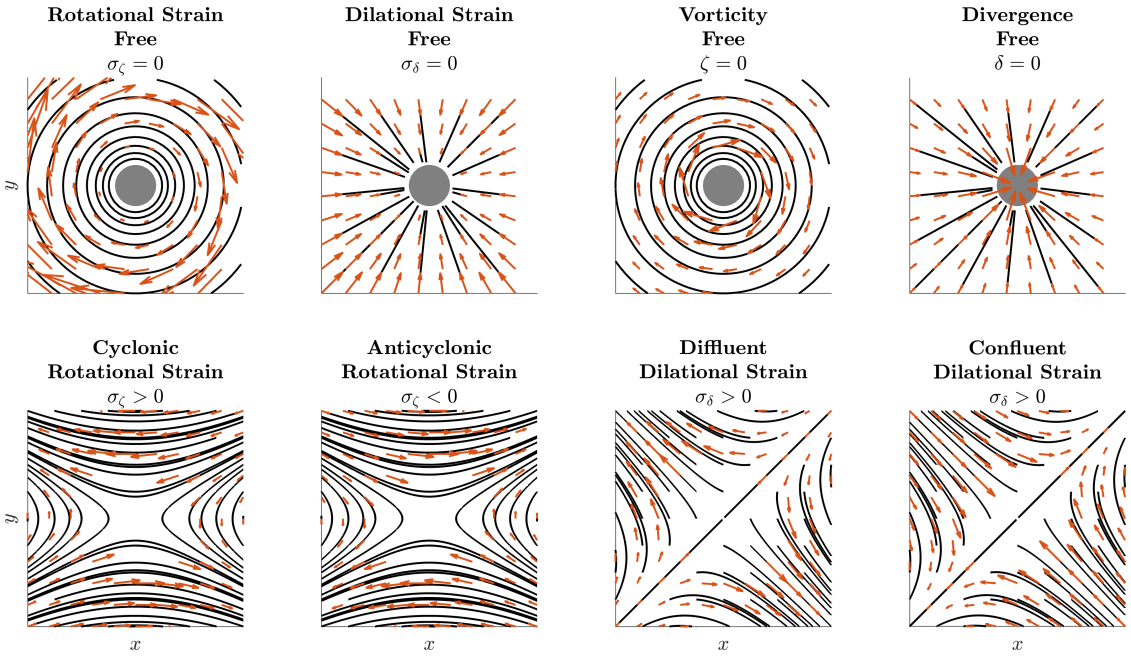

FIG. 2. Top row shows example flow fields for rotationally symmetric example flows, with no rotational strain, dilational strain, vorticity and divergence respectively. These flows all have singularities in the center, so this region is excluded. Bottom row shows example hyperbolic strain flow fields with enhanced rotational and dilational strain components of each sign. Note that the cyclonically (anticyclonically) curving region of the hyperbola is enhanced when $\sigma_\zeta > 0$ ($\sigma_\zeta < 0$). In the dilational strain, the entrance (exit) flow is more spread apart, leading to an overall confluence, with $\sigma_\delta < 0$ (diffluence, with $\sigma_\delta > 0$).

gradients in velocity and tracers are oriented perpendicular to the flow with some prescribed vertical structure, but no variability in the along-flow direction, motivated by thermal-wind balance. The flow-following frame provides a useful description of these flows, as it exactly distinguishes between across and along-flow gradients.

Frontogenesis is often analysed using the tendency equations for the horizontal buoyancy gradient magnitude $|\nabla_h b|^2$ and the horizontal velocity gradient magnitude $|\nabla_h \boldsymbol{u}|^2 = \partial_x u^2 + \partial_y u^2 + \partial_x v^2 + \partial_y v^2$ (McWilliams 2021). We ignore viscous and diffusive effects here for simplicity, but they can be easily incorporated. Barkan et al. (2019) conduct a scaling analysis to reduce the complexity of the equations for frontogenesis. They first consider a coordinate system oriented along front, then consider the case where the aspect ratio of their front is large. This scaling approach allows them to ignore gradients in the along-front direction to first order. The flow-following frame allows us to derive the same equations, in a way that reveals the underlying structure of the Barkan et al. (2019) assumptions.

If we assume that the gradients in the $\hat{s}$-direction can be neglected, then we get the following equations

$$|\nabla_h b|^2 \approx (\nabla_n b)^2, \tag{20}$$
$$|\nabla_h u|^2 \approx (\nabla_n V)^2 + (V\nabla_n \alpha)^2 = \mathfrak{s}^2 + \mathfrak{d}^2, \tag{21}$$
$$\zeta \approx -\nabla_n V = \mathfrak{s}, \tag{22}$$
$$\delta \approx V\nabla_n \alpha = \mathfrak{d}, \tag{23}$$

which replace vorticity by shearing and divergence by diffluence, both of which better describe the flow patterns within frontal systems that lack significant curvature. Deriving the evolution equations of these quantities (Appendix B), and neglecting the gradients in both the $\hat{s}$-direction, and the vertical $\hat{z}$-direction we get the evolution equations

$$\frac{1}{2}\frac{D(\nabla_n b)^2}{Dt} = -\mathfrak{d}(\nabla_n b)^2, \tag{24}$$
$$\frac{1}{2}\frac{D(\mathfrak{s}^2+\mathfrak{d}^2)}{Dt} = -\mathfrak{d}(\mathfrak{s}^2+\mathfrak{d}^2) + f\mathfrak{d}\mathfrak{s}_{ag}, \tag{25}$$
$$\frac{D\mathfrak{s}}{Dt} = -\mathfrak{d}\mathfrak{s} \tag{26}$$
$$\frac{D\mathfrak{d}}{Dt} = -\mathfrak{d}^2 + f\mathfrak{s}_{ag} - \mathfrak{s}\frac{\partial\alpha}{\partial t}. \tag{27}$$

These equations almost exactly mirror the Barkan et al. (2019) equations, apart from two differences. First of all, the Coriolis term is missing from the vorticity evolution equation: in Barkan et al. (2019), the RHS of the vorticity equation has vortex extension from planetary vorticity i.e. $D\zeta/Dt = -\delta(\zeta + f)$. The planetary vorticity term $f\delta$ is missing in our equations because shearing is not affected by the Coriolis force, whereas curving is (Appendix A). In Barkan et al. (2019), they also neglect the Coriolis term in the vorticity equation, citing the Turbulent Thermal Wind (TTW) balance, where the mixing terms will cancel it out. Our analysis shows that the TTW balance is not necessary to ignore the Coriolis effects on vorticity in the reduced frontogenesis model, as vorticity only takes the form of shearing in this model. The second difference is that we have retained the $\mathfrak{s}\frac{\partial \alpha}{\partial t}$ term in the divergence equation, as our only simplification has been to discount along-flow and vertical gradients. The frontal scaling of Barkan et al. (2019) does not account for a changing frontal direction with time, which might be forced by a larger scale advection, such as in fronts located around the edges of eddies. A changing frontal direction acts a potential source of confluence when coupled with shearing. Assuming a static angle α we recover the Barkan et al. (2019) model.

If we assume a geostrophic and barotropic flow, we can recover the frontogenetic equation for buoyancy (Eq. 24), without having to assume that velocity gradients are only in the $\hat{s}$-direction (Appendix B). Our analysis demonstrates that the *confluence* is a primary driver of frontogenesis, both at geostrophic scales and at submesoscales. We empirically demonstrate the importance of confluence in the NCOM model in Appendix B.

Lagrangian solutions for the system of equations (24)-(27), where the advective derivative is turned into a pure time derivative, have the form

$$\mathfrak{d} = \frac{\mathfrak{d}_0}{1 + \mathfrak{d}_0(\tau - \tau_0)}, \tag{28}$$

for time τ and initial diffluence $\mathfrak{d}_0$ at time τ_0, which implies a finite time singularity (blow-up) of the confluence and so also shearing during submesoscale frontogenesis. This frontogenesis can be arrested by frictional or diabatic effects, but also by along-flow gradients ∇_s which may disrupt the force balance in the equations (24)-(27). Therefore, we expect the signature of intense frontogenesis within the statistics of submesoscale velocity gradients should be high confluence, high shearing regions.

d. Eddies

Eddies are a ubiquitous feature of mesoscale and submesoscale flows, often defined and identified by their coherence in time. There are many possible eddy-identification methods, each implying a different definition of eddies. Common approaches rely on eddy closed contours of sea-surface height (Fang and Morrow 2003) or streamlines (Sadarjoen and Post 2000). However a simplistic identification tool, still often used, is the Okubo-Weiss parameter (Okubo 1970; Weiss 1991)

$$Q = \sigma^2 - \zeta^2. \tag{29}$$

For $Q < 0$, the vorticity dominates over the strain, which is associated with eddying flows. This parameter is tied to the notion of coherence via the eigenvalues of the velocity gradient tensor. Specifically, if $d\boldsymbol{X}$ is the separation distance between two particles under a purely horizontal and velocity field, we can write the first-order Taylor series expansion as

$$\frac{d}{dt} d\boldsymbol{X} \approx \Sigma d\boldsymbol{X}, \tag{30}$$

for the 2-D Jacobian velocity gradient matrix $\Sigma = [\partial u_i/\partial x_j]$, when $d\boldsymbol{X}$ is small. The matrix Σ has eigenvalues $\lambda_{1,2} = \delta \pm Q^{1/2}$, which leads to the local solution

$$d\boldsymbol{X}(t) \approx d\boldsymbol{X}(0) e^{\frac{1}{2}(\delta \pm Q^{1/2})t}. \tag{31}$$

If $Q < 0$, the solution is oscillatory in time, representing the eddying motion of the particles. If, on the other hand $Q > 0$, particle separation increases exponentially, implying a strain-dominated regime and loss of coherence.

So the link between $Q < 0$ and eddies is based on the notions that (1) eddies are associated with large vorticity, and (2) the separation between particles should remain small within an eddy structure. However, as shown in Figure 2, it is possible to have a coherent eddy velocity structure (closed streamlines), with no vorticity, if the shear cancels out the curvature. In this case, $Q > 0$, but we might argue that the velocity structure defines an eddy. In this eddy, locally particles disperse, as they are sheared apart, but globally the particles are coherent, as the eddy loops them back around. This is made more obvious by writing the Okubo-Weiss in the flow-following frame,

$$Q = (\mathfrak{d} - \mathfrak{e})^2 - 4\mathfrak{c}\mathfrak{s} = \sigma_\delta^2 - 4\mathfrak{c}\mathfrak{s}. \tag{32}$$

The sign of Q depends on the relative signs of curving and shearing, which means that if shearing and curving have opposite signs, then $Q > 0$, but if they are of opposite signs, then $Q < 0$ only if $\mathfrak{c}\mathfrak{s} > \sigma_\delta^2/4$.

3. Data

a. S-MODE

The Submesoscale Ocean Dynamics Experiment was a series of field campaigns that took place in the California Current region from 2021 to 2023, with the goal of measuring submesoscale dynamics, and testing the capabilities of airborne observations for this purpose. We will

discuss data collected during the two Intensive Operational Periods (IOPs 1 and 2) in October 2022 and April 2023 respectively. We will discuss only three of the many publicly available data sources: DopplerScatt, an airborne radar Doppler scatterometer; surface drifters, deployed from the M/V Bold Horizon (IOP1) and the R/V Sally Ride (IOP2); and the Navy Coastal Ocean Model (NCOM), a 1 km resolution ocean model of the California Current which has assimilated data from the S-MODE campaign.

b. DopplerScatt

DopplerScatt is an airborne Doppler radar scatterometer, that uses pulse-coherent processing of a translating and rotating radar to measure the speed and amplitude of capillary waves on the sea surface using Ka-band radar ($\sim$ 1 cm wavelength). A geophysical model function is used to separate the ocean current signal from the capillary wave propagation and other phenomena that contribute to the measured capillary wave speeds, including gravity wave-capillary wave interactions (Rodríguez et al. 2018). The geophysical model function is inferred from comparison to in-situ ADCP measurements.

To calculate surface velocity gradients from DopplerScatt, we use processing parameters similar to those in Torres et al. (2024). Namely, we smooth the 200 m measured data to 4 km using a half-amplitude Gaussian filter (creating a 22-point filter window), and exclude all data with estimated surface current errors greater than $0.05\,\mathrm{m\,s^{-1}}$. In total we will synthesize 39 flights of DopplerScatt (16 flights for IOP1 and 23 for IOP2), for $\sim$ 1.5 million estimates of velocity gradients from a variety of atmospheric and oceanic conditions.

c. NCOM

The Navy Coastal Ocean Model (NCOM, Yu et al. 2023) was run with a horizontal resolution of 1 km and 100 vertical layers, with daily three-dimensional variational (3DVar) data assimilation across the S-MODE study region. In this manuscript we will restrict our attention to the S-MODE operational area, during the months of October 2022 and April 2024 for comparison to in-situ data. We only use data from NCOM within a box illustrated in Figure 3 with a red dashed line, chosen to encompass most of the DopplerScatt flights for direct comparison, and avoid continental shelf data with shallow water depths, where the dynamics are noticeably different.

d. Drifters

A total of 192 surface drifters were release during S-MODE IOPs 1 (55) and 2 (137). Most of these drifters were of the CARTHE model (Novelli et al. 2017), that are drogued at 40 cm depth, with some of the Microstar model (Ohlmann et al. 2005) that are drogued at 1 m depth. Both forms of drifter report latitude and longitude approximately every 5 minutes, giving an average horizontal displacement of 80 m across both campaigns. We use temporal Gaussian averaging of 1 km ($\sim$1 hour), 5 km ($\sim$ 5 hours), and 25 km ($\sim$ 1 day), to reduce noise and test the effect of changing scale. We include a moving 6-point Hampel filter with 3 standard deviations to remove spikes in speed due to GPS position uncertainty.

The drifters follow the horizontal surface ocean current, so provide natural measurements of the advective derivatives in horizontal velocity $D_h\boldsymbol{u}_h/Dt$. On the 5 minute timescale, we assume a frozen-flow, which implies that Lagrangian changes arise from along-stream variability (∇_s) rather than temporal evolution (∂_t) . As the velocity spectrum is red, and dominated by large scale currents (see Figure 3 for sample trajectories), this is a relatively good assumption at the 5 minute sampling rate. Therefore we can infer the along-flow gradients of curvature $\mathfrak{c}$ and extension $\mathfrak{e}$ from Lagrangian drifter observations. Measuring the across-flow gradients ($\mathfrak{s},\mathfrak{d}$) would require differentiation between drifters (e.g. Essink et al. 2018; Donnet et al. 2025), which we leave for future studies. Note that the flow-following frame representation lends itself to natural drifter data description – none of the "traditional metrics" (ζ,δ,α) can be fully derived from a drifter trajectory.

4. Results

We have shown theoretically that the flow-following frame allows us to more naturally describe frontogenetic dynamics (high confluence, high shearing), and eddying processes (high curving). To demonstrate these theoretical results, we first consider the statistical distributions of our velocity gradients in the S-MODE data. To provide additional context we will then discuss the representation of inertial oscillations in these statistics, and finally internal waves more broadly.

a. PDFs

The statistical distribution of velocity gradients for the S-MODE data from DopplerScatt and from NCOM have many similarities with previous submesoscale-resolving observations. The flow-following diagnostics allow us to explore these joint statistics along the new dimensions, potentially offering additional insight. Figure 4 shows a cyclonically-skewed vorticity distribution in both model and observations and a slightly negatively skewed divergence distribution, in keeping with expectations. NCOM tends to have less intense velocity gradients than DopplerScatt. There are multiple possible reasons for this discrepancy. The DopplerScatt data has measurement noise that will contribute to spurious velocity gradients, as well as time-space aliasing resulting from repeat sampling. The additional errors will produce some gradients larger than physical measurements, so DopplerScatt may be biased

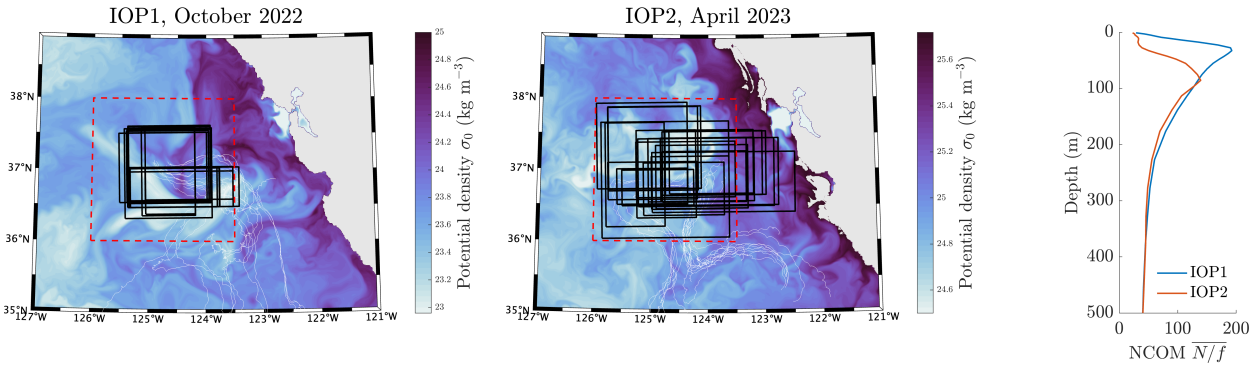

FIG. 3. a),b) Potential density from NCOM for the S-MODE study region for the intensive operating periods (IOPs) 1 (a) and 2(b). Black boxes denote the area measured each day by the DopplerScatt instrument. The red box denotes the region of NCOM we sample from for our statistical comparison. c) Mean stratification profile from NCOM during IOP1 and IOP2.

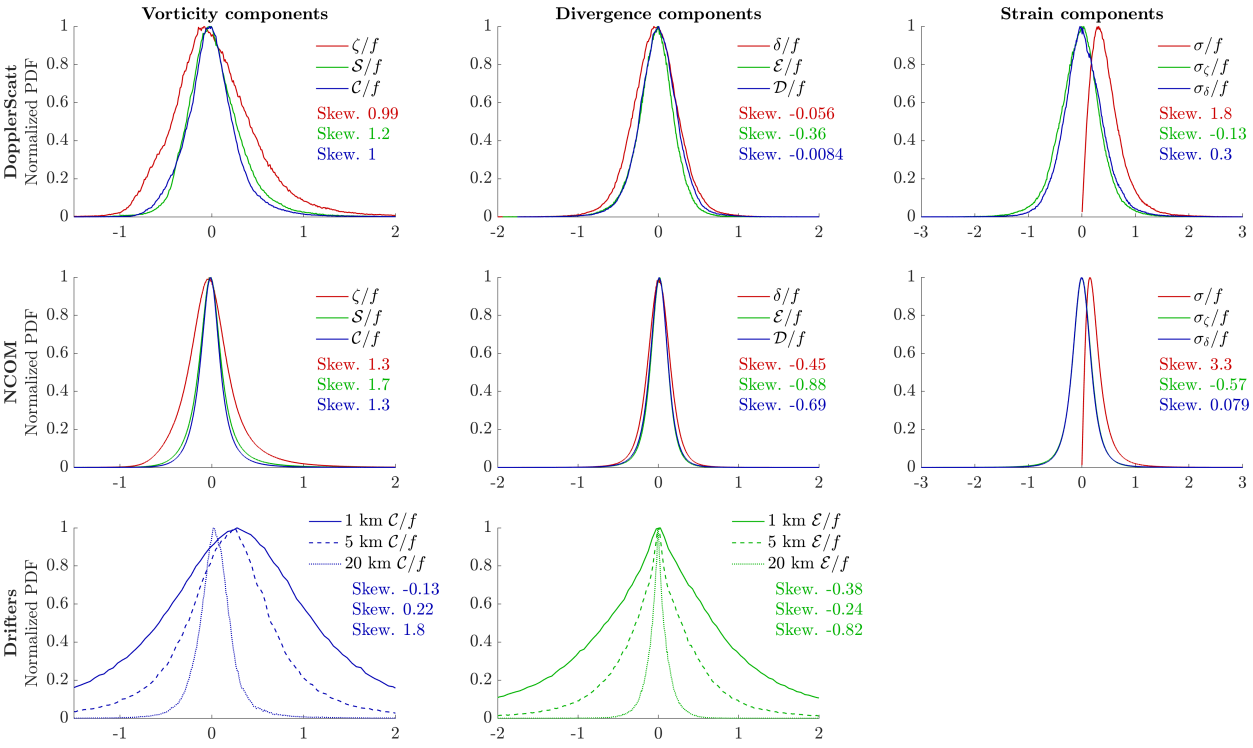

FIG. 4. One dimensional PDFs of the velocity gradients (normalized by f) from DopplerScatt (top row), NCOM (middle row) and drifters (bottom row). Left column shows the PDFs of vorticity ζ, shearing $\mathfrak{s}$ and curving $\mathfrak{c}$. Middle column shows the PDFs of divergence δ, extension $\mathfrak{e}$ and diffluence $\mathfrak{d}$, c) shows PDFs of the total strain σ, rotational strain σ_ζ and dilational strain σ_δ. The bottom row shows PDFs for just the curving and extension gradients that can be calculated from drifter data, presented at three different smoothing lengths (1 km, 5 km and 20 km).

high in terms of the velocity gradient distribution. NCOM has a spatial resolution of 1 km, however its effective resolution is likely larger than that, potentially up to 10 km. This would preclude the more intense velocity gradients from the simulation, as usually appear in high-resolution model runs (Balwada et al. 2022). Both the model and observations show velocity gradients smaller than what has been observed in the Gulf Stream (Shcherbina et al. 2013), which is by design of the S-MODE campaign, to investigate a more globally-representative submesoscale regime, in terms of velocity gradient intensity. Using a higher-resolution ROMS model simulation of the 2013 period in the S-MODE region we get very similar PDFs to those shown with NCOM (not shown), suggesting model resolution may not explain the discrepancy.

DopplerScatt has a similar distribution of along-stream velocity gradients to the drifter data when filtered at 5 km. The drifters show a slightly larger standard devia-

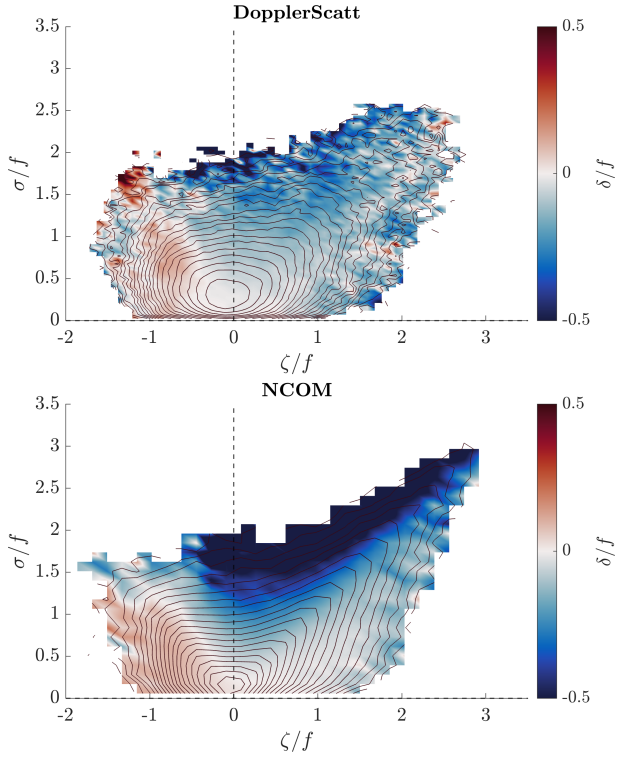

FIG. 5. Two-dimensional joint PDFs of vorticity versus strain, coloured by a conditional average of divergence, for DopplerScatt (upper) and NCOM (lower).

tion, with a more sharply peaked distribution, particularly for the extension term. The drifters have a sampling that is biased towards regions of convergence, which may explain the mean curvature vorticity being cyclonically biased compared to the DopplerScatt and NCOM data, due to the association between convergence and cyclonic vorticity. This bias may give rise to the large skew in the distribution of extension at small scales, although another likely explanation is that the frozen-field approximation is not applicable at 1 km scales, and so temporal gradients in the flow are being interpreted as spatial gradients (inertial veering). However, when we smooth the drifter velocity derivatives to 24 hours (~20 km), the distribution appears much more similar to NCOM. NCOM likely does not represent well the high-frequency waves (near-inertial oscillations and internal gravity waves) that exist in the real ocean, for which the frozen field approximation (equating spatial derivatives with time derivatives) may break down. Therefore, the method of drifter velocity gradient diagnostics may require mostly balanced dynamics to function, which appears to hold for averaging at slower than inertial timescales.

The differences in statistics of the curving versus shearing components in Figure 4 is somewhat subtle, with each of the components at first order following the same distribution. In particular, this means that the shearing ($-\nabla_n V$) and curving ($V\nabla_s \alpha$) are both skewed cyclonically, in model and observation. Only the curving component is directly affected by the Coriolis force (see Appendix A), so the shearing is amplified from alternative processes, likely the frontogenetic feedback, leading to a higher level of skew for shearing than curving. The extension ($\nabla_s V$) and diffluence ($V\nabla_n \alpha$) terms look very similar, however in both model and observations we have a slightly wider distribution for the diffluence than the extension, and a slightly larger skew for the extension. The two components of strain are close to normally distributed, with mean around zero, implying a roughly equal proportion of both cyclonic and anticyclonic rotational strain, and both divergent and convergent dilational strain. There is a slight asymmetry, with more anti-cyclonic rotational strain, and more convergent dilational strain.

Despite the differences between NCOM and DopplerScatt in velocity gradient distribution intensity, the joint PDFs in Figure 5 show similar inter-dependencies of the vorticity, strain, and divergence. Both model and observations show the characteristic cyclonic bias of vorticity, along the $\zeta = \sigma$ line. The conditionally-averaged divergence shows similar patterns between DopplerScatt and NCOM, with the convergence highest in the high-strain region. The divergence occurs primarily in the region where anti-cyclonic vorticity dominates over strain.

In Figure 6, we re-imagine the classic vorticity versus strain diagram in terms of shearing and curving, for both DopplerScatt and NCOM. The red lines denote the axes of vorticity, and rotational strain, as labeled. There is an asymmetry in both model and observations between the shearing and the curving, with both components displaying a cyclonic (+ve) bias. Within the model, the shearing is somewhat more asymmetric than the curving, however this result does not hold within the DopplerScatt observations. The cyclonic bias in shearing is in keeping with the original interpretation of Shcherbina et al. (2013) who associated strong cyclonic vorticity with frontal shearing, as discussed above in section c. The asymmetry in curving, on the other hand, is not well explained by current theories of frontogenesis. Curving asymmetry could result from a conversion of enhanced cyclonic shear into cyclonic curving via the exchange processes discussed in Bell and Keyser (1993) (Appendix A), or from a separate 'cyclogenetic' feedback from enhanced vortex extension, similar to the process within straight fronts.

There is a large convergence associated with strain dominance in Figure 6, as in Balwada et al. (2022), but more specifically this convergence is associated with the rotational-strain $\sigma_\zeta = \mathfrak{c} - \mathfrak{s}$ not the total straining $\sigma = (\mathfrak{c} - \mathfrak{s})^2 + (\mathfrak{d} - \mathfrak{e})$. That means that convergence is observed for cyclonic shearing and anti-cyclonic curving in both observations and model. The flow-following diagnostics reveal a new insight: strong divergence tends to

occur only when $\mathfrak{c} \leq 0$ *and* $\mathfrak{s} \leq 0$; strong convergence tends to happen when $\mathfrak{c}$ and $\mathfrak{s}$ are $O(f)$ and oppositely signed.

Within straight fronts, we neglect the curving (section c), so the processes causing this convergence is not accounted for by purely straight-front theories. Within NCOM there is convergence associated with cyclonic curving and anticyclonic shearing, however this associated is notably missing from the DopplerScatt data. The real ocean contains larger high-frequency variability in the form of internal waves and near-inertial oscillations than in NCOM, so we will investigate these possible drivers effects below.

To confirm the association between high shearing and high curving regions with strong convergence, we have plotted the joint PDFs for curving and shearing velocity gradients, conditioned on a bracket of divergence values in Figure 7. The strongly convergent regions $\delta/f \approx -1$ are indeed dominated by large cyclonic shearing and curving. However, the uncommon and extreme values of convergence in NCOM ($\delta/f \approx -3.25$) mostly sit close to the line of constant weak vorticity, and varying rotational strain. These regions are also highlighted as the most highly divergent regions in the PDF of ($\delta/f \approx 3.25$).

The enhanced curving regions could be associated with eddy edges, during eddy adjustments as in Wu et al. (2025), meandering jets, as in Bower and Rossby (1989) and MacKinnon et al. (2021), or on the edges of symmetrical eddies, where frontogenesis can occur with radially-oriented straining Shakespeare (2016), or in idealized flows that have not yet been described in the literature. To give a visualisation of the difference between curving and shearing flows, we have plotted a snapshot from NCOM in Figure 8 where we have subset the regions where curving dominates and where shearing dominates respectively. We have plotted contours of the Okubo-Weiss parameter Q given in section 2d, to indicate eddy core regions. Both shearing and curving fronts appear on the edges of eddies, and within some relatively straight looking fronts, which confounds simple narratives around the nature of these curving-dominated regions. However, it is clear that most of the high vorticity structures are dominated by either shear or curvature, suggesting that there are two distinct frontogenetic processes at work. We have argued that the enhancement of shearing is reasonably explained by the Barkan et al. (2019) model, but the frontogenetic enhancement of curvature still requires an idealized understanding. The model of Shakespeare (2016) accounts for curving fronts, however it assumes a radially-symmetric flow, which discounts the frontogenetic enhancement of curvature.

Viewing the same velocity gradient distribution from a different point of view, Figure 9 plots the diffluence against the extension component, with conditional averaging of vorticity. In these PDFs, the red lines denote the directions of divergence and dilational strain. As in the total strain plot (Figure 5), the skew towards convergent flow in high-strain regions is obvious. However, in the DopplerScatt observations there is less asymmetry for dilational strain than in the model. The most intense convergence is associated with contraction and confluence, but in this region the vorticity is significantly weaker than in the high strain-high convergence regions, which skew the joint PDF significantly.

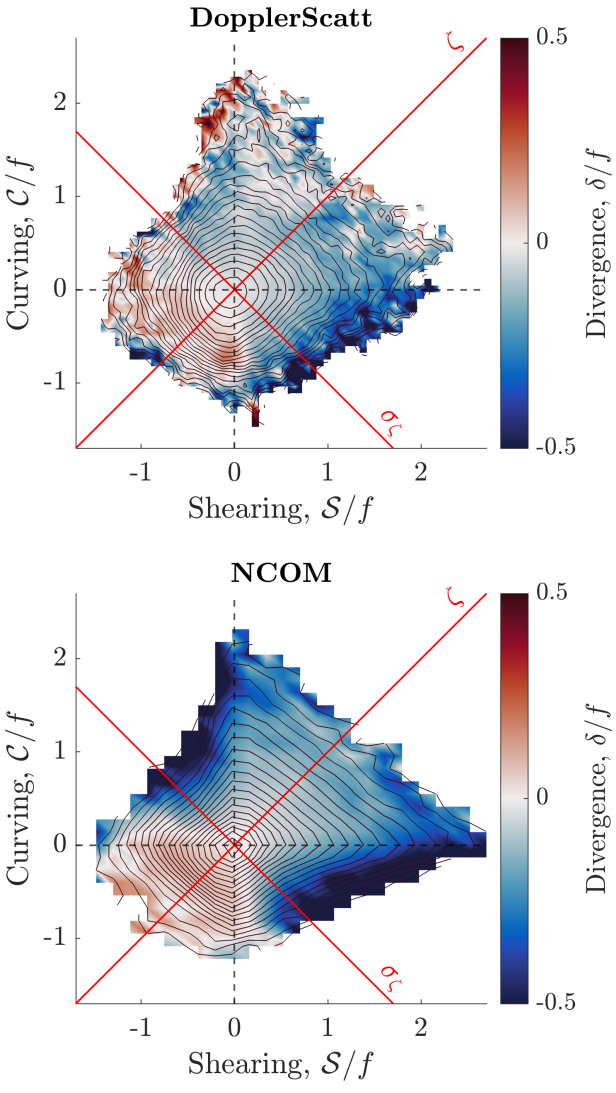

FIG. 6. Two-dimensional joint PDFs of shearing $\mathfrak{s}$ and curving $\mathfrak{c}$, coloured by a conditional average of divergence δ, for DopplerScatt (upper) and NCOM (lower). The red lines indicate coordinate axes for vorticity $\zeta = \mathfrak{c} + \mathfrak{s}$ and rotational strain $\sigma_\zeta = \mathfrak{c} - \mathfrak{s}$.

5. Idealized dynamics

To explore the possible dynamical drivers of the statistical distributions of curving velocity gradients at the submesoscale, we have run a range of idealized experiments with varying physics. In this section we will briefly

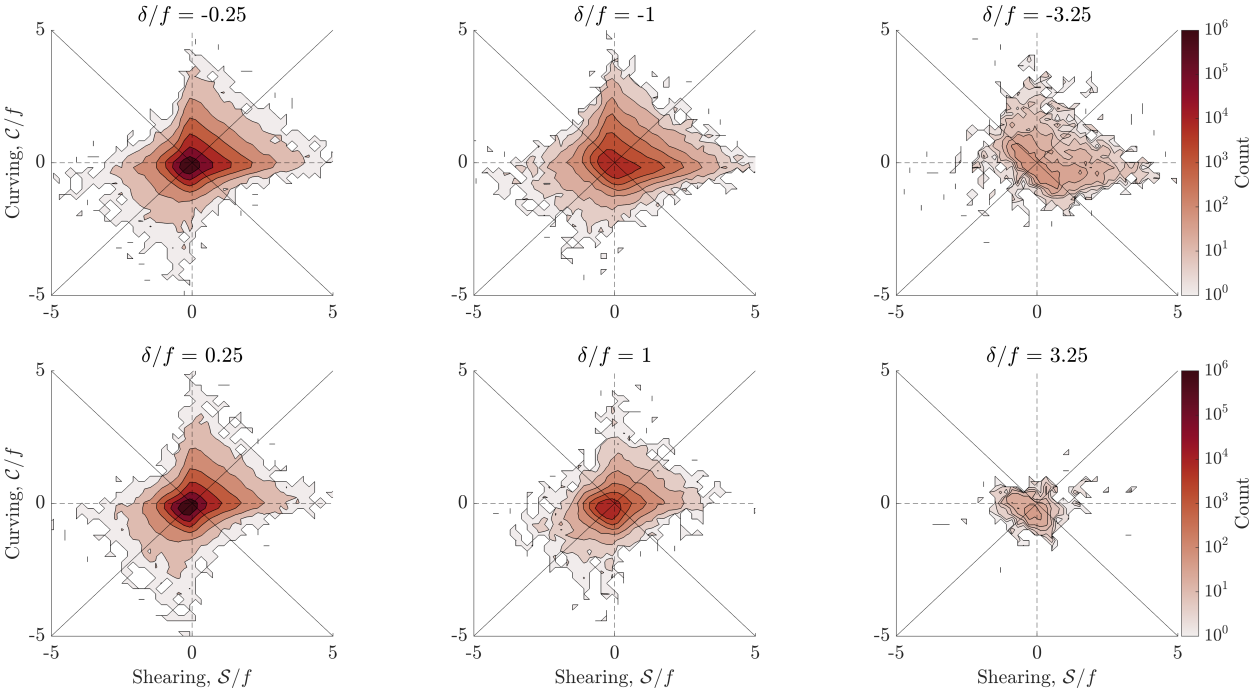

FIG. 7. The level sets of velocity gradient statistics for set values of the normalized divergence δ/f. These level sets are shown as Joint PDFs of curving $\mathfrak{c}$ versus shearing $\mathfrak{s}$ velocity gradients, averaged over bins of a certain divergence value, indicated in the title of each subplot. The top row shows convergent joint PDFs, and the bottom row shows divergent joint PDFs.

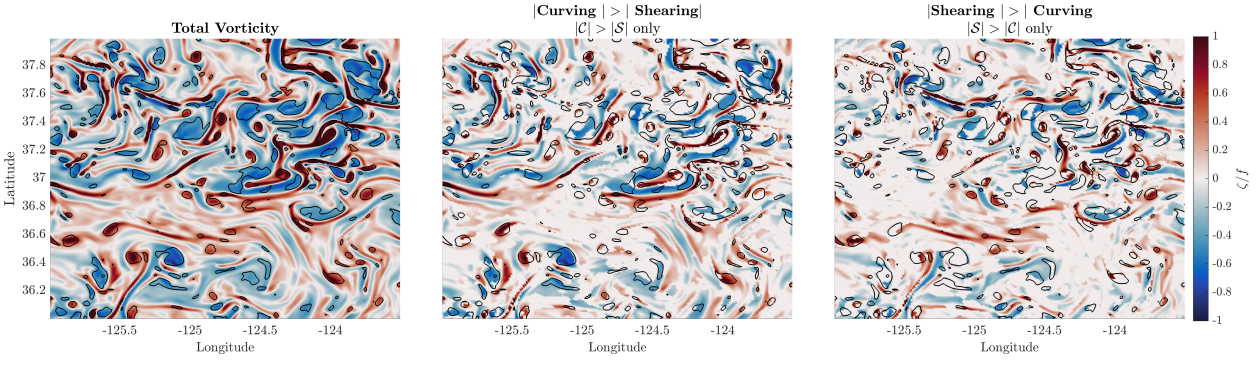

FIG. 8. Snapshot of the vorticity field from the NCOM study area outlined in Figure 3 during IOP2. Leftmost plot shows the full vorticity field, the middle plot shows a subset of the vorticity field, only in the region where the curving dominates over the shearing, and the rightmost plot shows only the regions where the shearing dominates over the curving. In all plots, we have plotted contours of $Q = \sigma_\delta^2 - 4\mathfrak{c}\mathfrak{s} = 0.1f^2$ to isolate eddy centers.

describe each experiment in turn, then give its results and discussion.

a. Surface quasi-geostrophy

At synoptic scales, ocean dynamics are relatively well approximated by geostrophic flow. At the mesoscale, quasi-geostrophy (QG) is often used as a next-order description to approximate the dynamics. QG, which is theoretically valid for low-Rossby number flow, allows the approximation of vertical velocities from the omega equation. With the advent of satellite altimetry, it became increasingly desirable to proscribe a vertical structure within the QG model, in order to infer vertical fluxes from surface data from satellite products. We will utilise the so-called surface quasi-geostrophic (SQG) model, which supposes an exponential decay of density, to demonstrate the difference between low-Rossby number, large scale dynamics and submesoscale dynamics. We run an SQG model (see Appendix C), initialising with the surface buoyancy dis-

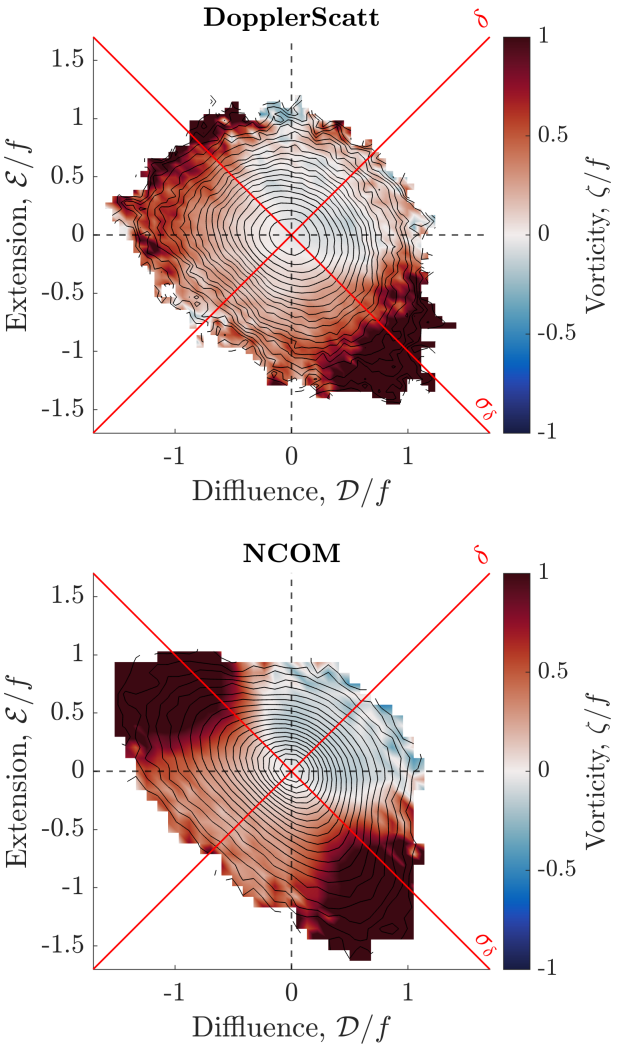

FIG. 9. Two-dimensional joint PDFs of diffluence $\mathfrak{d}$ and extension $\mathfrak{e}$, coloured by a conditional average of vorticity ζ, for DopplerScatt (upper) and NCOM (lower). The red lines indicate coordinate axes for divergence $\delta = \mathfrak{d} + \mathfrak{e}$ and dilational strain $\sigma_\delta = \mathfrak{d} - \mathfrak{e}$.

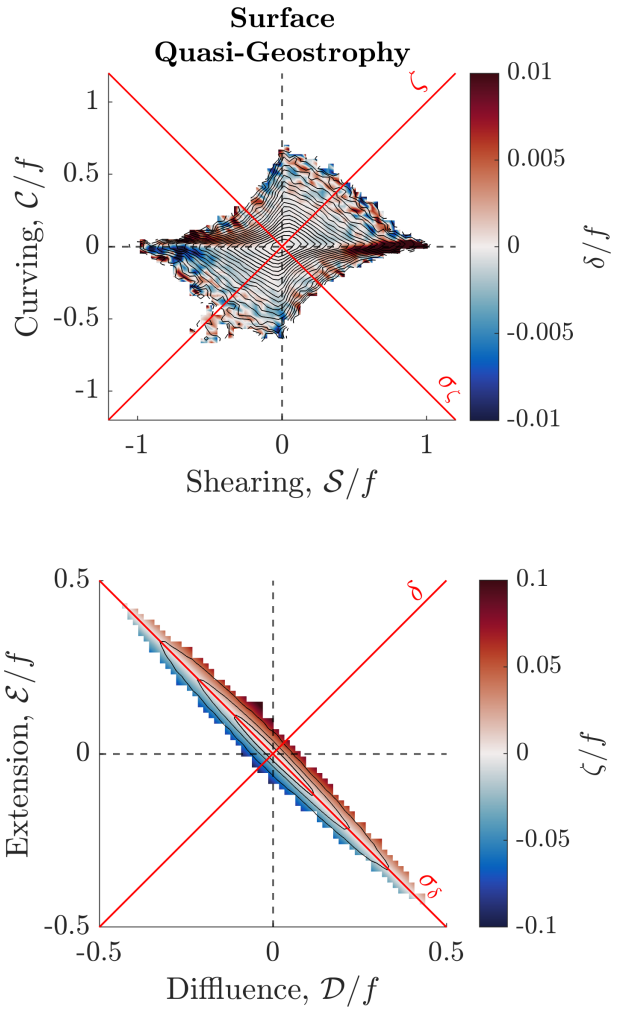

FIG. 10. Two-dimension joint PDFs of velocity gradients for Surface Quasi-Geostrophic simulations. Upper plot shows joint PDFs of shearing, colored by divergence versus curving, as in Fig. 6, and lower plot shows joint PDFs of diffluence versus extension, colored by vorticity, as in Fig. 6.

tribution from NCOM, and fitting the decay scale of the exponential buoyancy distribution to NCOM.

Figure 10 shows the output of the SQG model as a distribution in shearing-curving space and extension-diffluence space. Comparing these to the NCOM distributions in Figure 6 and 9, you can see that the magnitudes are significantly smaller. The SQG data do not quite reach $O(f)$ in vorticity or strain, compared with up to $2f$ in the submesoscale data. Notably, the divergence is much smaller, not quite reaching $0.1f$. Interestingly, the dilational strain is still comparatively large. This means that SQG dynamics almost always balance extension with confluence or contraction with diffluence.

At the submesoscale, the QG-omega equation is often used as a first approximation of the vertical velocity distribution. However, as demonstated in our comparison of SQG and NCOM velocity gradients, the distributions of velocity gradients, in particular the divergence, are very different to those in the primitive-equation simulation, both in terms of magnitude (at least an order of magnitude smaller), and distribution. The SQG dynamics do not produce any of the submesoscale correlations between high strain-regions (either high shearing or high curving) and convergence. The anti-correlation between extension and diffluence shows that the geometry of QG flows is very different to that of fully developed submesoscale flows.

b. Internal waves

At frequencies between the Coriolis frequency and the buoyancy frequency, the spectra of horizontal velocities

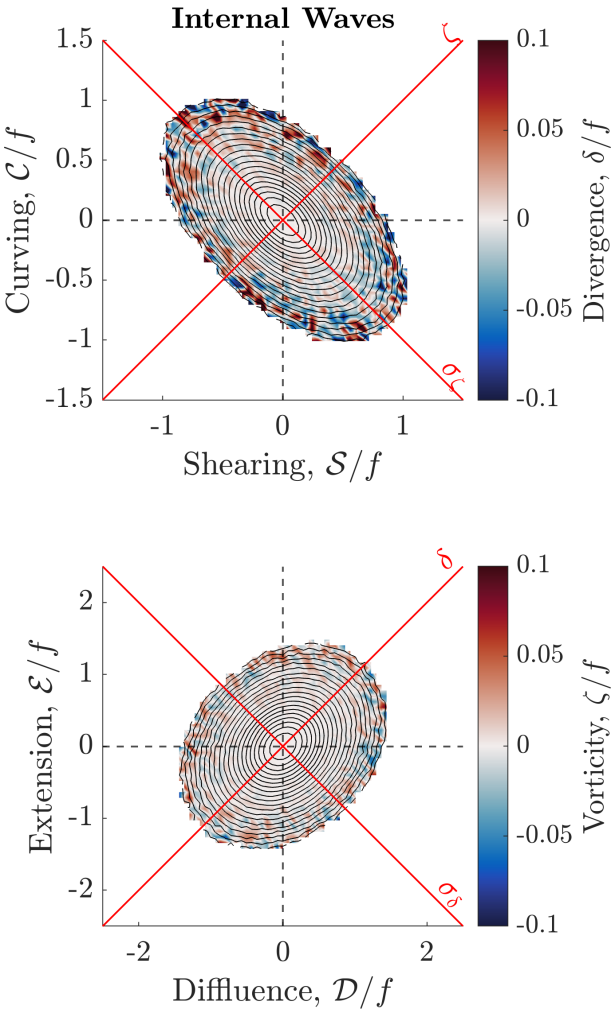

FIG. 11. Two-dimension joint PDFs of velocity gradients for Garrett-Munk spectrum internal wave simulations. Upper plot shows joint PDFs of shearing, colored by divergence versus curving, as in Fig. 6, and lower plot shows joint PDFs of diffluence versus extension, colored by vorticity, as in Fig. 6.

are heavily impacted by internal waves. The Garrett-Munk spectrum (GM, Garrett and Munk 1975) provides a universal spectrum for internal waves, dependent only on stratification and latitude, that has relatively accurate results globally (Garrett and Munk 1979). In the surface ocean there are rapidly changing dynamics and horizontal density gradients which alter the internal wave dynamics, away from the universal GM spectra (e.g., Samelson and Farrar 2024), but to get a first impression of the effect of internal waves on the statistics of velocity gradients, we will proceed with a GM spectrum. Note that NCOM does not have a full spectrum of internal waves, so real and aliased internal wave signals may help explain some of the discrepancy between observations and model.

To create a synthetic distribution of internal waves, we used GLOceanKit to simulate a GM spectrum of waves, using an exponential stratification, fit to match NCOM. We then calculated the velocity gradients from the simulated wavefield and calculated joint PDFs of the velocity gradients.

The magnitude of the velocity gradients, shown in Figure 11, are all of a similar order of magnitude to the full submesoscale realization in Figures 5-9. This indicates that some portion of the observationally observed gradients will likely be due to internal wave variability. However, the velocity gradient distribution from GM is more symmetric compared to that from e.g. quasi-geostrophic motions. There is slightly more rotational strain relative to vorticity, shown in Figure 11, and slightly more divergence than dilational strain. As we decrease the rotation rate, the asymmetry between vorticity and rotational strain increases, tending toward the vorticity-free non-rotating wave case. However, there is no significant pattern of divergence associated with the curving and shearing, as we see within a dynamic submesoscale.

Part of the discrepancy between observations and model in Fig. 9 may be explained by internal waves present in the observation but not in NCOM. Adding white noise to the NCOM velocity fields decreases the conditionally-averaged divergence, bringing it further into line with the observations (not shown). The internal wave velocity gradients are skewed in terms of rotational strain, and of a similar magnitude to observations. Therefore, because their divergence is essentially white noise, their signal may decrease the observed convergence for large rotational strain values, exactly where the observations and model disagree. Instrument noise in DopplerScatt may also provide a similar effect of decreasing the large convergence values.

c. *Wind-driven flow and inertial oscillations*

Under an impulse of wind forcing, the surface ocean can undergo inertial oscillations, which are often observed in the trajectories of drifters (Figure 3). To understand the effects of these oscillations on the statistics of velocity gradients, we can take a simple "slab layer" model for linear wind effects with a linear damping r (Pollard and Millard 1970), as

$$\frac{\partial \boldsymbol{u}}{\partial t} + r\boldsymbol{u} + f\hat{\boldsymbol{z}}\times\boldsymbol{u} = \frac{\boldsymbol{\tau}}{\rho_0 H}, \tag{33}$$

for the wind stress vector $\boldsymbol{\tau}$, assumed to act homogeneously over vertical depth scale H, which for a slab model can be identified with the mixed layer depth. We can break this

balance down in the flow-following frame as

$$\frac{\partial V}{\partial t} + rV = \frac{\tau_s}{\rho_0 H}, \tag{34}$$

$$V\frac{\partial \alpha}{\partial t} + fV = \frac{\tau_n}{\rho_0 H}. \tag{35}$$

Clearly the damping factor only affects the speed of the flow, not its angle. In the absence of wind stress and damping, the velocity vector would maintain a constant speed V with a linearly increasing angle α (at rate f), hence the simple inertial oscillation.

To estimate the possible the contribution of inertial oscillations within our observations, we apply the simple slab model point-by-point to the wind-field from ERA5. The results of this are given in Figure 12. The joint PDF is extended in the directions of the flow-following frame velocity gradients, giving a diamond shape, rather than a circle as in the Garrett-Munk spectrum of internal waves. There is a relatively large divergence associated with cyclonic and anti-cyclonic shearing, but not curving. In the extension-diffluence comparison, we have a slight asymmetry to the extension, with more positive extension and less negative contraction. The magnitude of the linear wind-driven currents are all an order of magnitude less than the submesoscale gradients displayed above, so we would not expect them to have a strong direct effect on the submesoscale velocity gradient statistics. However, they do give us an indication that there is some structure in the velocity gradient distributions for wind-driven flows, which when extended to include the non-linear ocean background, could have significant effects. The non-linear wind-driven flow in a flow-following frame is left as a topic for future studies.

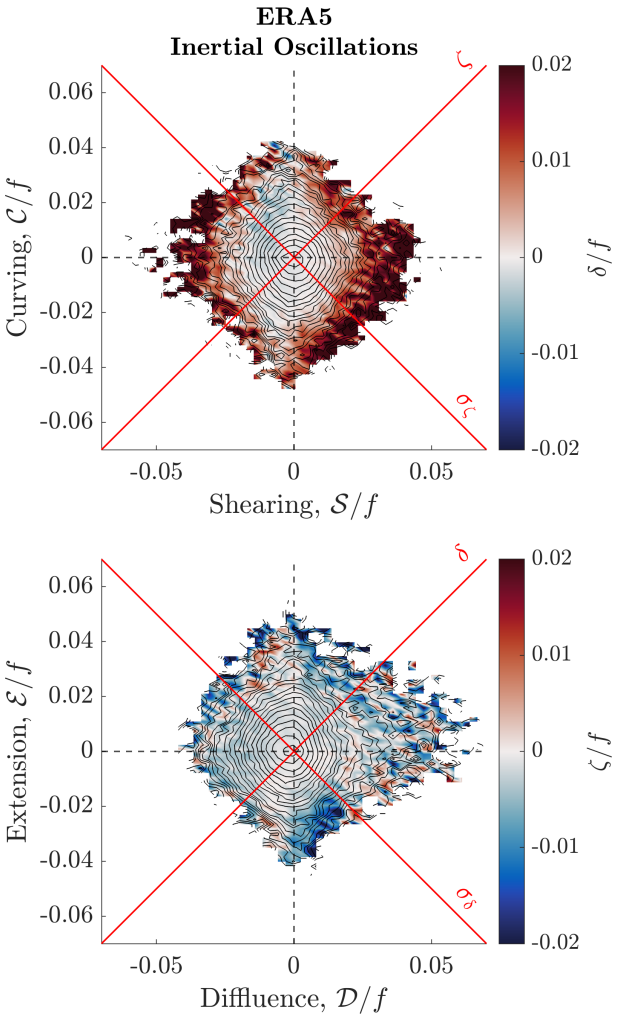

FIG. 12. Two-dimension joint PDFs of velocity gradients for slab model simulations for inertial oscillations under ERA5 wind forcing. Upper plot shows joint PDFs of shearing, colored by divergence versus curving, as in Fig. 6, and lower plot shows joint PDFs of diffluence versus extension, colored by vorticity, as in Fig. 6.

6. Discussion and Conclusions

We have demonstrated that there are distinct submesoscale features in the statistics of velocity gradients, when broken down into curvature components. In particular, we find that the strain decomposition into a rotational strain and dilational strain are useful tools in analysing a variety of idealised ocean dynamics that contribute to submesoscale variability. The distinct distributions of the idealized processes (internal waves, quasi-geostrophic dynamics and inertial oscillations) suggest that more specific information can be gained from observations of ocean velocity gradients regarding driving processes. We suggest that these distributions are a good heuristic for a given set of observations to determine their governing process.

We showed that confluence and shearing are the only velocity gradients that have a direct dynamical effect on frontogenesis/frontolysis in the generalized model of Barkan et al. (2019). Enhanced regions of confluence and shearing regions are present within NCOM and DopplerScatt observations, in keeping with previous observations of enhanced straight fronts at the submesoscale. However, we also observed an enhancement of cyclonic curving as well as shearing. Previous authors have highlighted the potential for curving regions to be subduction hotspots, and our observation of enhanced convergence in these regions confirms this hypothesis. The features associated with curving dominating over shearing, and vice versa, appear to be diverse. Around the edges of eddies and at large curving fronts, both shearing and curving can dominate. Although some regions have alternating curving and shearing dominance (likely related to vorticity exchange, as in Bell and Keyser 1993), most high vorticity regions are dominated by either curving or shearing. The exact mechanisms for enhanced curvature vorticity are not well understood, al-

though the example of a splitting eddy provides one mechanism (Middleton et al. 2025).

Air-sea interactions appear sensitive to the distinction between different forms of vorticity and divergence. This has already been shown by e.g. Wenegrat and Thomas (2017), but our idealized experiments lend weight to this conclusion. There are significant divergences associated with wind-driven shearing, which when extended to nonlinear wind response may provide a mechanism for obduction via Ekman pumping at the submesoscale.

Another benefit of the flow-following frame, is that it is the natural frame for much of our Lagrangian sampling in the ocean. We demonstrated this by considering the statistics of velocity gradients from drifters, which agreed relatively well with those from DopplerScatt provided sufficient averaging. Extension and curving are the natural velocity gradients that can be inferred from drifters without considering gradients between driters (e.g. Tarry et al. 2021). A natural follow up to our work would be to extend our analysis to the global drifter database, to examine the global variability in drifter velocity gradient statistics. At larger scales, these methodologies could also be applied to the argo float program, where coarse velocities can be inferred from argo drift with time.

Overall, the flow-following frame reveals the diversity of flow patterns in the submesoscale. Our work motivates further studies of exotic idealized flows, beyond straight frontal jets and circularly-symmetric eddies, in order to properly represent and understand the zoo of possible dynamics at the submesoscale.

Acknowledgments. We thank the many contributors to the S-MODE campaign for their significant work in creating this comprehensive dataset. In particular, we thank Ernesto Rodriguez and Eric D'Asaro, who helped lead S-MODE and the decision making about sampling strategies; we thank the DopplerScatt team (Ernesto Rodriguez, Dragana Perkovic-Martin, Alex Wineteer, Hector Torres), the NRL NCOM team (Joseph D'Addezio and Gregg Jacobs), and all of the participants in the S-MODE cruises and planning activities. This work was supported by grants from NASA and the Office of Naval Research.

Data availability statement. All data used within this manuscript can be accessed via NASA's PODAAC https://podaac.jpl.nasa.gov/S-MODE . In particular we used the 'S-MODE NCOM Model Output Version 1', 'S-MODE DopplerScatt Level 2 Ocean Winds and Currents Version 2' and 'S-MODE L2 Position Data from Surface Drifters Version 1' datasets.

APPENDIX A

Velocity gradient budgets

To calculate the budgets for the flow-following frame velocity gradients, we follow the methodology of Bell and Keyser (1993). The components themselves can be calculated from Cartesian coordinates, as follows

$$\mathfrak{s} = -\nabla_n V = -\frac{1}{V^2}\left(u^2u_y - v^2v_x - uv(u_x - v_y)\right), \quad \text{(A1)}$$

$$\mathfrak{c} = V\nabla_s\alpha = \frac{1}{V^2}\left(u^2v_x - v^2u_y - uv(u_x - v_y)\right), \quad \text{(A2)}$$

$$\mathfrak{e} = \nabla_s V = \frac{1}{V^2}\left(u^2u_x + v^2v_y + uv(v_x + u_y)\right), \quad \text{(A3)}$$

$$\mathfrak{d} = V\nabla_n\alpha = \frac{1}{V^2}\left(u^2v_y + v^2u_x - uv(v_x + u_y)\right), \quad \text{(A4)}$$

for partial derivative denoted by subscripts. There is no need to calculate Lagrangian trajectories to calculate heuristics like the radius of curvature of trajectories or streamlines, as these quantities can be calculated explicitly using cartesian gradients.

The budgets for these four components are as follows,

$$\frac{D\mathfrak{s}}{Dt} = -\mathfrak{s}\overbrace{(\mathfrak{e}+\mathfrak{d})}^{\delta} + \nabla_n w\frac{\partial V}{\partial z} - \left[\mathfrak{e}\left(f + \frac{\nabla_n p}{V}\right) - \nabla_n(\nabla_s p)\right] \quad \text{(A5)}$$

$$\frac{D\mathfrak{c}}{Dt} = -(\mathfrak{c}+f)\overbrace{(\mathfrak{e}+\mathfrak{d})}^{\delta} - V\nabla_s w\frac{\partial\alpha}{\partial z} + \left[\mathfrak{e}\left(f + \frac{\nabla_n p}{V}\right) - \nabla_n(\nabla_s p)\right] \quad \text{(A6)}$$

$$\frac{D\mathfrak{e}}{Dt} = -\mathfrak{e}^2 + \mathfrak{s}\mathfrak{d} - \nabla_s w\frac{\partial V}{\partial z} + \left[\mathfrak{s}\left(f + \frac{\nabla_n p}{V}\right)\right] - \nabla_s^2 p \quad \text{(A7)}$$

$$\frac{D\mathfrak{d}}{Dt} = -\mathfrak{d}^2 + \mathfrak{s}\mathfrak{c} + f\underbrace{(\mathfrak{s}+\mathfrak{c})}_{\zeta} - V\nabla_n w\frac{\partial\alpha}{\partial z} - \left[\mathfrak{s}\left(f + \frac{\nabla_n p}{V}\right)\right] - \nabla_n^2 p + \mathfrak{d}\nabla_s p/V - \mathfrak{c}\nabla_n p/V, \quad \text{(A8)}$$

where the terms in square brackets are the exchange terms between shearing and curving, and extension and diffluence respectively.

APPENDIX B

Frontogenesis in the flow-following frame

To understand the general mechanism of frontogenesis, we consider the horizontal buoyancy gradient magnitude evolution equation in the flow-following frame, broken up

into the four velocity gradient contributions,

$$\frac{1}{2}\frac{D|\nabla_h b|^2}{Dt} = -[\mathfrak{e}\nabla_s b^2 - \mathfrak{s}\nabla_s b\nabla_n b + \mathfrak{c}\nabla_s b\nabla_n b + \mathfrak{d}\nabla_n b^2], \tag{B1}$$

Analogously, the horizontal velocity gradient magnitude evolution equation is

$$\begin{aligned}\frac{1}{2}\frac{D|\nabla_h \boldsymbol{u}|^2}{Dt} = -\Big[&\mathfrak{e}\left(|\nabla_s \boldsymbol{u}|^2 - V\nabla_s^2 p - \mathfrak{e}\nabla_s p\right)\\ &- \mathfrak{s}\left(\nabla_n \boldsymbol{u}\cdot\nabla_s \boldsymbol{u} - V\nabla_n\nabla_s p + \mathfrak{s}\nabla_s p\right)\\ &+ \mathfrak{c}\left(\nabla_n \boldsymbol{u}\cdot\nabla_s \boldsymbol{u} - V\nabla_s\nabla_n p - \mathfrak{c}\nabla_s p\right)\\ &+ \mathfrak{d}\left(|\nabla_n \boldsymbol{u}|^2 - V\nabla_n^2 p - \mathfrak{d}\nabla_s p\right)\Big]\end{aligned} \tag{B2}$$

In the simplest case of barotropic and geostrophic flow, we can remove the $\nabla_s b$ terms, using thermal wind balance $\nabla_s b = (\nabla_s p)_z + \alpha_z \nabla_n p$. There are no along-flow pressure gradients in geostrophic flow, and no changes in flow direction with depth in barotropic flow, so $\nabla_s b = 0$. Likewise, there are no vertical velocities, so we get the much simplified equations

$$\frac{1}{2}\frac{D|\nabla_h b|^2}{Dt} = -\mathfrak{d}|\nabla_h b|^2, \tag{B3}$$

$$\frac{1}{2}\frac{D|\nabla_h \boldsymbol{u}|^2}{Dt} = -\mathfrak{d}(V\nabla_n^2 p - |\nabla_n \boldsymbol{u}|^2), \tag{B4}$$

that demonstrate the importance of confluence for frontogenesis at large rotationally-controlled scales.

We demonstrate the breakdown of frontogenesis in the full NCOM buoyancy field in Figure B1, showing the time-averaged spatial map of the frontogenesis function, broken down by components on the left, and on the right we show the spatially averaged statistics, varying with time (mean in the upper panel, and standard deviation in the lower panel). The confluence term remains the most important contribution, even when submesoscale gradients are considered, as suggested within section 2c.

APPENDIX C

Surface quasi-geostrophic simulations

Within our surface quasi-geostrophic simulations, we solve the equations

$$\frac{\partial b}{\partial t} + J(\psi, b) = 0 \qquad \text{at } z = 0, \tag{C1}$$

$$\frac{\partial}{\partial z}\left(\frac{f^2}{N^2}\frac{\partial \psi}{\partial z}\right) + \nabla_h^2 \psi = 0, \tag{C2}$$

$$\hat{\psi}(k,l,z) = \frac{f}{N}\frac{1}{\kappa}\hat{b}(k,l,z)e^{\kappa N z/f}, \tag{C3}$$

where b is the buoyancy distribution, ψ is the 3D streamfunction, $J(\cdot,\cdot)$ is the Jacobian, f is the Coriolis parameter, N is buoyancy frequency, and $\hat{}$ denotes the Fourier transform.

We initialized the SQG model on a 250×250 km^2 periodic box, initialized with a snapshot of the NCOM surface buoyancy field at the beginning of IOP2. The SQG simulation was then run for 50 days. There is no continuous forcing in the SQG model, and so the flow quickly diverges from the NCOM velocity fields. However, the distribution of velocity gradients was relatively insensitive to alternative choices of initialization in our testing.

References

Archer, M., J. Wang, P. Klein, G. Dibarboure, and L.-L. Fu, 2025: Wide-swath satellite altimetry unveils global submesoscale ocean dynamics. *Nature*, **640 (8059)**, 691–696.

Balwada, D., J.-H. Xie, R. Marino, and F. Feraco, 2022: Direct observational evidence of an oceanic dual kinetic energy cascade and its seasonality. *Science Advances*, **8 (41)**, eabq2566.

Barkan, R., M. J. Molemaker, K. Srinivasan, J. C. McWilliams, and E. A. D'Asaro, 2019: The role of horizontal divergence in submesoscale frontogenesis. *Journal of Physical Oceanography*, **49 (6)**, 1593–1618.

Bell, G. D., and D. Keyser, 1993: Shear and curvature vorticity and potential-vorticity interchanges: Interpretation and application to a cutoff cyclone event. *Monthly weather review*, **121 (1)**, 76–102.

Bower, A. S., and T. Rossby, 1989: Evidence of cross-frontal exchange processes in the gulf stream based on isopycnal rafos float data. *Journal of Physical Oceanography*, **19 (9)**, 1177–1190.

Buckingham, C. E., J. Gula, and X. Carton, 2021: The role of curvature in modifying frontal instabilities. Part II: Application of the criterion to curved density fronts at low Richardson numbers. *Journal of Physical Oceanography*, **51 (2)**, 317–341.

Donnet, S., H. S. Huntley, M. Berta, L. Centurioni, L. Middleton, T. Özgökmen, P.-M. Poulain, and A. Griffa, 2025: Surface evolution and wind effects during a cyclonic eddy splitting event in the balearic sea. *EGUsphere*, **2025**, 1–31.

D'Addezio, J. M., and G. A. Jacobs, 2022: Scale-dependent ocean vertical correlations in the california current system. *Geophysical Research Letters*, **49 (22)**, e2022GL100 184.

Essink, S., A. Mahadevan, V. Hormann, and L. R. Centurioni, 2018: Understanding dispersion in the bay of bengal: A multi-drifter approach to estimate velocity gradients. *American Geophysical Union, Ocean Sciences Meeting*, RS14A–194, 194.

Fang, F., and R. Morrow, 2003: Evolution, movement and decay of warm-core leeuwin current eddies. *Deep Sea Research Part II: Topical Studies in Oceanography*, **50 (12-13)**, 2245–2261.

Farrar, J. T., and Coauthors, 2025: S-mode: the sub-mesoscale ocean dynamics experiment. *Bulletin of the American Meteorological Society*, **106 (4)**, E657–E677.

Garrett, C., and W. Munk, 1975: Space-time scales of internal waves: A progress report. *Journal of Geophysical Research*, **80 (3)**, 291–297.

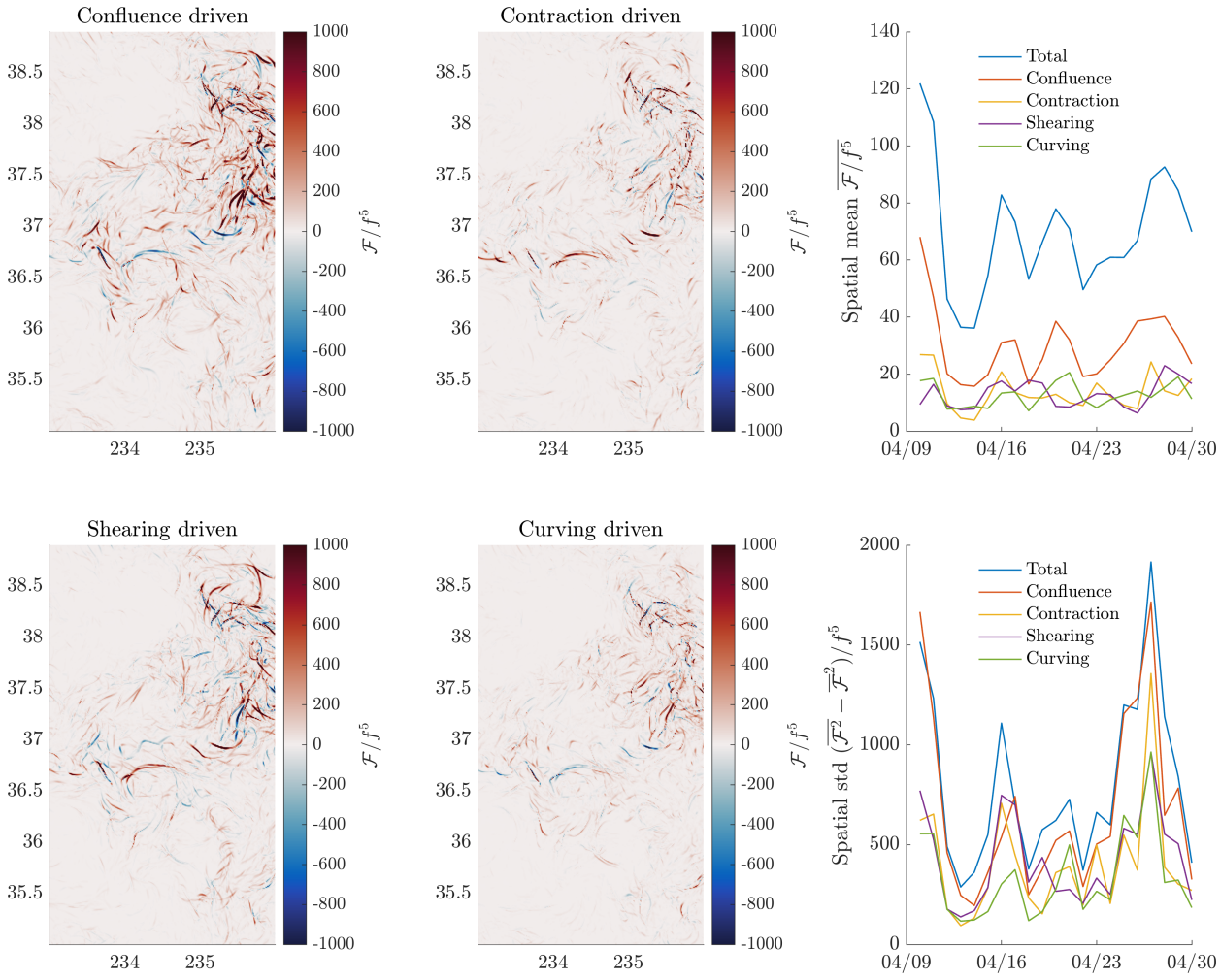

FIG. B1. Panels on the left show the time-averaged, normalized frontogenesis function $\mathcal{F}/f^5$ from NCOM during IOP2, broken down as the confluence-driven, contraction-driven, shearing-driven and curving-driven components. On the right we have the spatially averaged statistics, varying with time, of the same region shown on the left. The upper panel shows the mean, broken down by components, and the lower panel shows the standard deviation of the frontogenesis components.

Garrett, C., and W. Munk, 1979: Internal waves in the ocean. *Annual review of fluid mechanics*, **11 (1)**, 339–369.

Holton, J. R., and G. J. Hakim, 2012: *An introduction to dynamic meteorology*. Academic press.

Hoskins, B. J., 1982: The mathematical theory of frontogenesis. *Annual review of fluid mechanics*, **14 (1)**, 131–151.

Lévy, M., P. J. Franks, and K. S. Smith, 2018: The role of submesoscale currents in structuring marine ecosystems. *Nature communications*, **9 (1)**, 4758.

MacKinnon, J. A., and Coauthors, 2021: A warm jet in a cold ocean. *Nature communications*, **12 (1)**, 2418.

Mahadevan, A., 2016: The impact of submesoscale physics on primary productivity of plankton. *Annual review of marine science*, **8**, 161–184.

McWilliams, J. C., 2021: Oceanic frontogenesis. *Annual Review of Marine Science*, **13**, 227–253.

Middleton, L., and Coauthors, 2025: Observations of a splitting ocean cyclone resulting in subduction of surface waters. *Science advances*, **11 (30)**, eadu3221.

Novelli, G., C. M. Guigand, C. Cousin, E. H. Ryan, N. J. Laxague, H. Dai, B. K. Haus, and T. M. Özgökmen, 2017: A biodegradable surface drifter for ocean sampling on a massive scale. *Journal of Atmospheric and Oceanic Technology*, **34 (11)**, 2509–2532.

Ohlmann, J. C., P. F. White, A. L. Sybrandy, and P. P. Niiler, 2005: Gps–cellular drifter technology for coastal ocean observing systems. *Journal of Atmospheric and Oceanic Technology*, **22 (9)**, 1381–1388.

Okubo, A., 1970: Horizontal dispersion of floatable particles in the vicinity of velocity singularities such as convergences. *Deep sea research and oceanographic abstracts*, Elsevier, Vol. 17, 445–454.

Pallàs-Sanz, E., T. Johnston, and D. Rudnick, 2010: Frontal dynamics in a California Current System shallow front: 2. Mesoscale vertical velocity. *Journal of Geophysical Research: Oceans*, **115 (C12)**.

Pollard, R., and R. Millard, 1970: Comparison between observed and simulated wind-generated inertial oscillations. *Deep Sea Research and Oceanographic Abstracts*, **17 (4)**, 813–821, https://doi.org/https://doi.org/10.1016/0011-7471(70)90043-4.

Rodríguez, E., A. Wineteer, D. Perkovic-Martin, T. Gál, B. W. Stiles, N. Niamsuwan, and R. R. Monje, 2018: Ocean surface currents and winds using dopplerscatt. *IGARSS 2018-2018 IEEE international geoscience and remote sensing symposium*, IEEE, 1474–1476.

Sadarjoen, I. A., and F. H. Post, 2000: Detection, quantification, and tracking of vortices using streamline geometry. *Computers & Graphics*, **24 (3)**, 333–341.

Samelson, R., and J. Farrar, 2024: Models of the sea surface height expression of the internal-wave continuum. *Journal of Physical Oceanography*, **54 (10)**, 2099–2117.

Shakespeare, C. J., 2016: Curved density fronts: Cyclogeostrophic adjustment and frontogenesis. *Journal of Physical Oceanography*, **46 (10)**, 3193–3207.

Shcherbina, A. Y., E. A. D'Asaro, C. M. Lee, J. M. Klymak, M. J. Molemaker, and J. C. McWilliams, 2013: Statistics of vertical vorticity, divergence, and strain in a developed submesoscale turbulence field. *Geophysical Research Letters*, **40 (17)**, 4706–4711.

Spall, M. A., 1995: Frontogenesis, subduction, and cross-front exchange at upper ocean fronts. *Journal of Geophysical Research: Oceans*, **100 (C2)**, 2543–2557.

Srinivasan, K., R. Barkan, and J. C. McWilliams, 2023: A forward energy flux at submesoscales driven by frontogenesis. *Journal of Physical Oceanography*, **53 (1)**, 287–305.

Su, Z., J. Wang, P. Klein, A. F. Thompson, and D. Menemenlis, 2018: Ocean submesoscales as a key component of the global heat budget. *Nature communications*, **9 (1)**, 775.

Sullivan, P. P., and J. C. McWilliams, 2018: Frontogenesis and frontal arrest of a dense filament in the oceanic surface boundary layer. *Journal of Fluid Mechanics*, **837**, 341–380.

Tarry, D. R., and Coauthors, 2021: Frontal convergence and vertical velocity measured by drifters in the alboran sea. *Journal of Geophysical Research: Oceans*, **126 (4)**, e2020JC016 614.

Thomas, L. N., A. Tandon, and A. Mahadevan, 2008: Submesoscale processes and dynamics. *Ocean modeling in an Eddying Regime*, **177**, 17–38.

Torres, H. S., and Coauthors, 2024: Airborne observations of fast-evolving ocean submesoscale turbulence. *Communications Earth & Environment*, **5 (1)**, 771.

Viúdez, Á., and R. L. Haney, 1997: On the relative vorticity of the atlantic jet in the alboran sea. *Journal of physical oceanography*, **27 (1)**, 175–185.

Weiss, J., 1991: The dynamics of enstrophy transfer in two-dimensional hydrodynamics. *Physica D: Nonlinear Phenomena*, **48 (2-3)**, 273–294.

Wenegrat, J. O., and L. N. Thomas, 2017: Ekman transport in balanced currents with curvature. *Journal of Physical Oceanography*, **47 (5)**, 1189–1203.

Whalen, C. B., and K. Drushka, 2025: Global distribution and governing dynamics of submesoscale density fronts. *Journal of Physical Oceanography*, **55 (10)**, 1831–1845.

Wu, W., L. Middleton, D. R. Tarry, E. A. D'Asaro, and A. Mahadevan, 2025: Curvature-induced subduction in a cyclonic eddy. *Journal of Physical Oceanography*.

Yu, J., C. A. Blain, P. J. Martin, and T. J. Campbell, 2023: Two-way nesting in a split-implicit ocean model: Ncom. *Journal of Atmospheric and Oceanic Technology*, **40 (7)**, 865–883.